

II

Experiments and analysis tools

5 Nuclei in collision

5.1 Heavy-ion research programs

The energy content available in the nuclear collision is the main factor in which experimental facilities differ from each other. The ultra-relativistic nuclear-collision systems we are considering are identified in table 5.1. For the maximum possible mass number up to $A_{\max} \simeq 200$, we show the fixed-target maximum beam energy per nucleon E_{P}^{\max} [A GeV]; for colliders, we present in this line the equivalent projectile energy. Similarly, we show the CM energy in the nucleon–nucleon system $\sqrt{s_{\text{NN}}}$ [GeV], which is twice the nominal beam energy of the RHIC and LHC collider systems. We also show the total $\sqrt{s_{\text{AA}}}$ [GeV] energy in the interaction region, allowing for the maximum mass number A of the beam. The final line refers to the rapidity ‘gap’ Δy . We will discuss these variables in the following sections.

Δy is defined as the difference between the rapidities of projectile and target. In laboratory fixed-target experiments, $y_t = 0$, and Δy is the rapidity of the projectile y_p . Using the definition of rapidity Eq. (5.4), we have

$$\cosh \Delta y = E_{\text{p}}/m_{\text{p}}. \quad (5.1)$$

For head-on interactions occurring at rest in the laboratory, at the collider facilities, $\Delta y/2$ is the projectile (target) rapidity of each beam, which is evaluated using, e.g., Eq. (5.1) again.

A convenient way to represent the data of table 5.1 is shown in Fig. 5.1: the solid line depicts the CM energy per pair of nucleons, $\sqrt{s_{\text{NN}}}$, as a function of the rapidity y . The horizontal distance between the two branches of the solid line is the projectile–target rapidity gap Δy . The shaded areas correspond to the accessible CM energies, $\sqrt{s_{\text{NN}}}$, at ex-

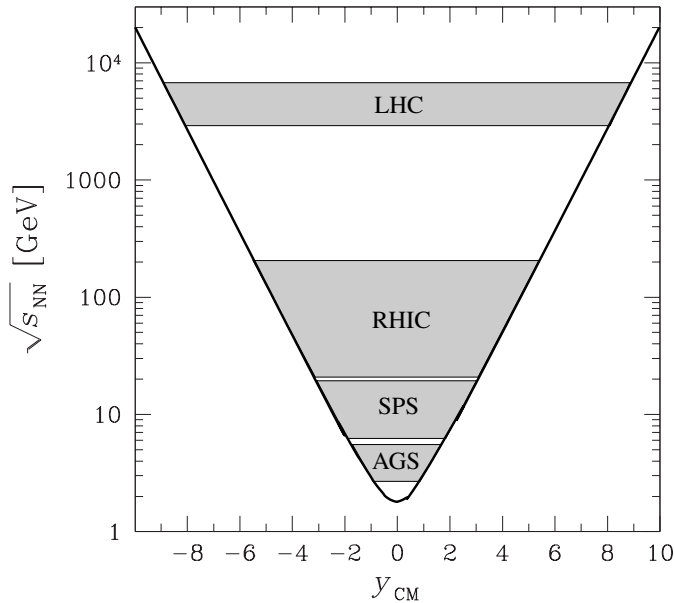


Fig. 5.1. $\sqrt{s_{NN}}$ (vertical axis) of various accelerators as a function of the projectile and target rapidities seen from the CM frame. Shaded areas: energy ranges accessible at the various accelerators.

perimental facilities that are in operation and under construction today.

As the energy increases, the rapidity gap Δy between projectile and target opens up as we see in Fig. 5.1. In the central rapidity region, we can study conditions of matter without having to account for particles spilled from the projectile and target fragments, which are known experimentally to spread over about two units of rapidity. Two extreme cases are illustrated qualitatively in Fig. 5.2, in which we sketch the distribu-

Table 5.1. Parameters of existing ultra-relativistic heavy-ion beam facilities and those under construction.

	AGS	AGS	SPS	SPS	SPS	RHIC	RHIC	LHC
Start year	1986	1992	1986	1994	1999	2000	2001	2006
A_{\max}	^{28}Si	^{197}Au	^{32}S	^{208}Pb	^{208}Pb	^{197}Au	^{197}Au	^{208}Pb
E_{P}^{\max} [A GeV]	14.6	11	200	158	40	0.91×10^4	2.1×10^4	1.9×10^7
$\sqrt{s_{NN}}$ [GeV]	5.4	4.7	19.2	17.2	8.75	130	200	6000
$\sqrt{s_{AA}}$ [GeV]	151	934	614	3.6×10^3	1.8×10^3	2.6×10^4	4×10^4	1.2×10^6
$\Delta y/2$	1.72	1.58	2.96	2.91	2.22	4.94	5.37	8.77

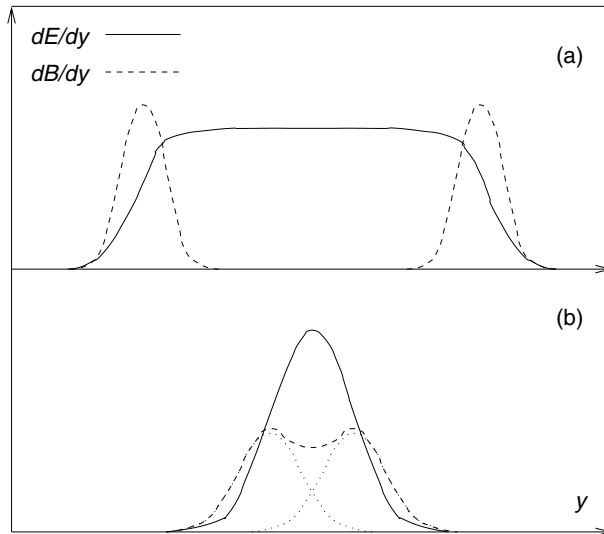


Fig. 5.2. Rapidity distributions of energy (solid lines) and baryon number (dashed lines) (in a qualitative representation): (a) for a ‘Transparent’ reaction mechanism; and (b) for full stopping in the collision.

tions of the energy (solid lines) and baryon number (dashed lines), as functions of the rapidity.

In the baryon-punch-through case, shown in Fig. 5.2(a), which was investigated by Bjørken [73], see section 6.4, the colliding nuclei are leaving a trail of energy between the projectile–target rapidity, but the baryon number continues to move out of the collision zone, apart from the down-shift in projectile and target rapidities necessary for conservation of energy.

The stopping limit, implicit in the work of Fermi [121] and described by Landau [173, 175], is shown in Fig. 5.2(b): both the particle multiplicity (energy) and the baryon number are centered around the central rapidity y_{CM} . The projectile and target baryons will, under the most extreme circumstance of complete stopping, lose all memory about the initial state, and in this limit there should in particular be little, if any, difference between the distributions of energy and baryon number in the longitudinal and transverse directions with respect to the collision axis.

We now survey the nuclear-collision experiments that are currently operating or under development. These include in particular the CERN–SPS heavy-ion program which continues a 15-year-long tradition in the so-called North Area (NA) in fixed-target mode with energy range up to $200A$ GeV for up to $A \simeq 100$ and dropping to $158A$ GeV for neutron-rich projectiles such as Pb. At higher energies, we have the beginning of the experimental program at the RHIC collider, and in the near future there

will be one at the LHC. The RHIC allows head-on collisions of two Au ions, each carrying energy in the range (10–100)A GeV. Results from the initial 65A-GeV run will be described and a glimpse of first 100A-GeV results is presented as this book goes to press. Compared with the SPS energies, the available CM energy per nucleon has been increased by an order of magnitude and accordingly the densities of matter reached are more extreme. Since the laboratory frame is also the CM frame in a collider experiment, the greatly increased particle density is distributed more evenly in all spatial directions.

We begin with the CERN–SPS research program*.

- The experiment NA45.2 investigates primarily the production of electron–positron pairs and of direct photons, continuing the research program of NA45 carried out with S-beams. Both experiments observe dielectron pairs and compare results with expectations based on p–p reactions. The current experimental set-up consists of a double spectrometer covering a region near mid-rapidity with full azimuthal coverage. Electrons are identified in two ring-imaging Čerenkov detectors (RICH).
- The experiment NA49, which had as its predecessor experiment NA35, uses several time-projection chambers (TPCs) for large-acceptance tracking of charged particles. Its current objective is to explore in greater detail the excitation function of strangeness near the possible threshold for the formation of the QGP phase. NA49 is at present the only experiment at the SPS capable of measuring many global observables required to characterize the nature of heavy-ion collisions as the energy is varied.
- The experiment NA57 continues the research program of experiments WA97, WA94, and WA85, all of which studied the production of (multi) strange hadrons in the central rapidity region, with particular emphasis on the production of strange antibaryons. NA57 is completely differently instrumented compared with the WA series and provides an important cross-check for all the results. It comprises silicon pixel tracking of hadrons in a magnetic field, and its results are based primarily on reconstruction of decays of strange hadrons.
- The experiment NA60 attempts detection of charmed hadrons, to complement the earlier study of suppression of production of J/Ψ by its predecessors NA50 and NA38. The NA50 muon spectrometer is complemented by a completely redesigned target area using radiation-tolerant silicon pixel detectors. The NA50 experiment studied dimuons pro-

* For further details consult the following CERN web pages:

<http://greybook.cern.ch/programmes/SPS.html>; and see also http://greybook.cern.ch/programmes/EXP_NAM.html, for all CERN experiments, including those completed.

duced in Pb–Pb and p–A collisions. The muons are measured in the former NA10 spectrometer, which is shielded from the target region by a beam stopper and absorber wall. The observed muons traverse 5 m of BeO and C.

- The completed experiment WA98 will be repeatedly mentioned in that which follows: WA98, which had as predecessors WA80 and WA87, which addressed the measurement of photons, but also measured the global production of charged hadrons. It comprised, in particular, a 10 000-module lead-glass spectrometer, which now is incorporated into the PHENIX detector (see below), yielding high-precision data on π^0 and η at mid-rapidity within a large range of transverse momenta $0.3 \text{ GeV}/c > P_{\perp} > 4.5 \text{ GeV}/c$ for π^0 . Detailed comparison of photons with the production of charged particles allowed also an evaluation of the photon enrichment potentially due to direct radiance from QGP.

We now turn to review the experimental research program at the BNL. Four experiments are at present taking data at the RHIC[†]. They are designed to allow both a survey of the reactions occurring in this hitherto unexplored condition of matter and an in-depth study of the properties of the deconfined QGP phase. We review the first results from the year-2000 run in section 9.5. The experiments currently under way are the following.

- **BRAHMS (Broad Range Hadron Magnetic Spectrometer)** is designed to measure hadronic particles inclusively (that is, to measure one particle at a time irrespective of what else is happening, when the system is triggered), over a wide range of rapidity ($0 < \eta < 4$) and transverse mass (up to 30 GeV). It consists of two (forward and mid-rapidity), magnetic focusing charged-particle (π^{\pm} , K^{\pm} , p, \bar{p}) spectrometer arms, which can be set to the desired angular acceptance window.
- **PHENIX (Pioneering High Energy Nuclear Interaction Experiment)** is a detector optimized to observe photons and dilepton pairs (γ , e^{\pm} and μ^{\pm}). It comprises a central detector made of an axial field magnet and two almost identical arms placed on the left and right of the magnet, each covering a window of ± 0.35 units of pseudorapidity. Each arm comprises several detector subsystems: the important goal of the central detector is observation of dielectrons at high mass resolution, allowing one to detect changes in the properties of decaying vector mesons (e.g., $J/\Psi \rightarrow e^+e^-$, $\phi \rightarrow e^+e^-$). The electro-magnetic calorimeter allows one to measure low- p_{\perp} photons near $y = 0$. Hadron detection in the silicon vertex detector, for $-2.65 < \eta < 2.65$, will allow studies of

[†] For RHIC experiments, see <http://www.rhic.bnl.gov>.

the distribution of charged hadrons (without identification of particles) on an event-by-event basis. First results from this subsystem obtained in the RHIC 2000 run have recently been published [16].

- **PHOBOS**, a scaled down ‘satellite’ of MARS (**M**odular **A**rray for **R**HIC **S**pectra), is a very small (in comparison) arrangement of silicon-based detectors that will allow one to study low-momentum particles within the complete (pseudo)rapidity interval $-5.4 < \eta < 5.4$, aiming to explore global event structure. PHOBOS has published the first results from the RHIC 2000 run on particle multiplicity [49], as well as the RHIC 2001 run [50].
- **STAR (Solenoidal Tracker at RHIC)** is a (large) 4π primarily hadronic-particle detector, with a 4-m-diameter and 4-m-long solenoidal 0.5-T magnetic-field volume, comprising as the main charged-particle-tracking device a TPC with inner radius 50 cm and outer radius 200 cm, with 45 planes of tracking. This allows a pseudorapidity coverage of $-2 \leq \eta \leq +2$, and the design allows for a lower particle-momentum cutoff at 60 MeV/ c . In addition, the inner silicon vertex tracker (SVT) is surrounding the interaction region between 5 and 15 cm, facilitating observation of the production of strangeness. The time-of-flight array, $\simeq 2.5$ m from the primary interaction vertex, will help identify charged particles. The outside electromagnetic calorimeter (EMC) aims to measure jets of particles, fluctuations, and high- p_{\perp} phenomena. The high tracking resolution facilitates reconstruction of unstable hadronic resonances. First results on central production of antiprotons [19] and anisotropy of particle multiplicity (elliptical flow) [15] have been published.

Still much more extreme matter conditions will be reached when the LHC collider is completed (<http://lhc.web.cern.ch/lhc/>) and the equivalent laboratory energy of $E_{\text{p}}^{\text{max}} \simeq 2 \times 10^{16}$ eV reaches into the domain of highest cosmic-particle energies, where the cosmic flux begins to decrease unusually rapidly. This ‘knee’ in cosmic flux as a function of the energy is below the high end of the LHC energy. At the LHC there will be initially three major detectors, ATLAS, CMS, and ALICE. ALICE is the dedicated heavy-ion experiment. CMS is intended to measure dilepton spectra under heavy-ion operation conditions. The ATLAS collaboration is exploring the potential of its detector in the heavy-ion environment.

- **ALICE (A Large Ion Collider Experiment)**[‡]. It comprises a TPC as a main tracking device of charged particles with an inner radius of 1 m and an outer radius of 2.5 m, and a length along the beam direction

[‡] See for further details the web page <http://www1.cern.ch/Alice>.

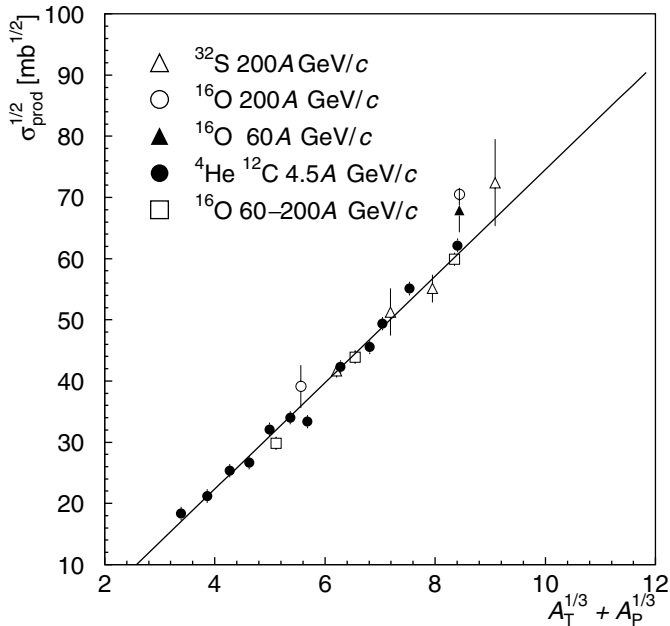


Fig. 5.3. The square root of the inelastic reaction cross section, $\sqrt{\sigma}$, as a function of the geometric size of interacting nuclei, $A_T^{1/3} + A_P^{1/3}$, for various collision partners, after [37].

of 5 m, covering the pseudorapidity interval $-0.9 < \eta < 0.9$. The high-resolution inner tracking system consists of five concentric cylindrical layers with radii from 7.5 to 50 cm around the beam pipe and allows the study of decays of charmed particles. An electro-magnetic calorimeter and a dilepton arm complement this very large and universal detector.

5.2 Reaction energy and collision geometry

On intuitive grounds, we expect that, for the short-range hadronic interactions, the collision geometry determines the amount of matter participating in nuclear collisions. The collision geometry is a very important and carefully explored subject. For an in-depth discussion of the importance of collision geometry, we refer the reader to the extensive body of work for hadron–hadron and hadron–nucleus interactions [184, 190].

The earliest experimental heavy-ion results confirmed the role of this simple geometric picture of nuclear-collision reaction dynamics [201]. The reaction radius, defined as the square root of the reaction cross section, rises linearly with the geometric size of the colliding nuclei, described by the sum of their radii, which is proportional to $A^{1/3}$, as is shown in

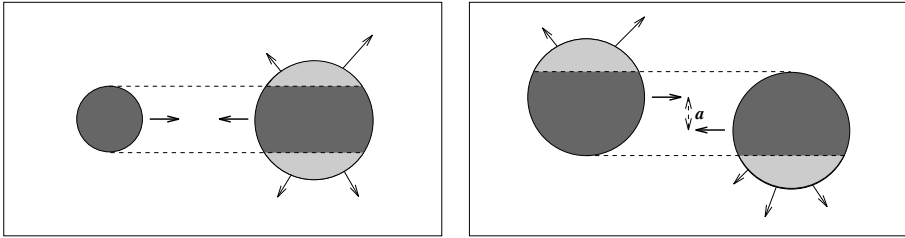


Fig. 5.4. A geometric illustration of nuclear collision. Left: small sulphur or aluminium nuclei colliding with much heavier lead or gold targets (correct relative scale). Right: symmetric collision of large nuclei at impact parameter a .

Fig. 5.3. This result confirms that the colliding nuclei need to ‘touch’ each other for local deposition of energy and baryon number to occur.

We show the central collision of sulphur or aluminium nuclei colliding with much heavier lead or gold targets in Fig. 5.4 (left-hand side). On the right-hand side, the symmetric slightly off-center collision with lead or gold is illustrated using the correct relative scale – we can see how important it is to assure that, in this system, the collision is geometrically as central as possible, in order to minimize the number of spectator (non-interacting, or partially interacting) nucleons. In symmetric collisions, only in a quite rare situation in which the impact parameter a is very small do we truly have the benefit of the largest possible region of interaction of the projectile and target, and do not encounter complications arising from spectator matter ‘polluting’ the experimental data.

A quantity of considerable importance is the energy content of the colliding system, which must be, by virtue of conservation of energy, the energy content of the final-state many-body system. The Lorentz invariant quantity we can form from the energy and momentum of the colliding projectile (p) and target (t) is

$$\sqrt{s_{pt}} \equiv \sqrt{(E_p + E_t)^2 - (\vec{p}_p + \vec{p}_t)^2}. \quad (5.2)$$

In the CM frame where by definition $\vec{p}_p + \vec{p}_t = 0$, $\sqrt{s_{pt}}$ is recognized as the available energy content of the projectile–target reaction, the CM energy. The quantity \sqrt{s} is thus the available reaction energy. Since it is an invariant, \sqrt{s} can be evaluated in any reference frame. It is natural to generalize this definition to any number of particles:

$$\sqrt{s^{(n)}} \equiv \sqrt{\left(\sum_{i=1}^n E_i\right)^2 - \left(\sum_{i=1}^n \vec{p}_i\right)^2}. \quad (5.3)$$

For $n = 1$, we see that \sqrt{s} is just the mass of a particle, i.e., its energy content at rest. The conservation of energy assures that, when a particle

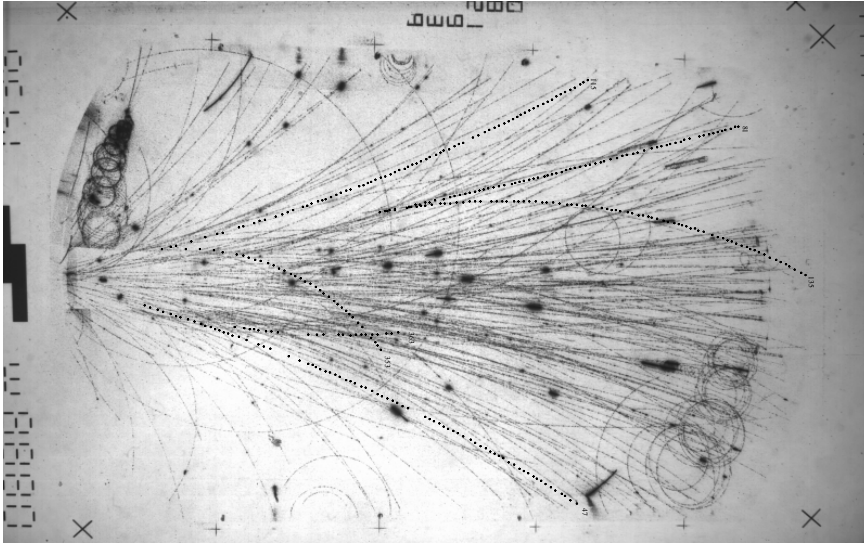


Fig. 5.5. A streamer-chamber picture of a S–Ag collision taken at 200A GeV (NA35 experiment [115]) showing the multiplicity of charged particles bent up and down in magnetic fields (with decays of neutral strange particles identified by superposed dashed lines).

decays, the final state comprising any number of particles n has the same \sqrt{s} . Conversely, $\sqrt{s^{(n)}}$ is also the (Lorentz invariant) mass of the ancestor system of the final-state n -body system, as determined by the momentum four vectors $p_i^\mu = (E_i, \vec{p}_i)$ of the particles produced.

This final-state energy described by Eq. (5.3) must be delivered by the colliding nuclei, see Eq. (5.2). $\sqrt{s^{(n)}}$ is also the invariant intrinsic rest energy (mass) of the fireball of dense matter, measured in terms of the participating energy and momentum of the colliding nuclei. Both these measures are jointly used in experiments to characterize a collision interaction: for example, the absence of the forward energy/momentum of the beam in the so-called zero-degree calorimeter (ZDC) can be correlated to the energy found in particles emitted in a direction transverse to the collision axis, see section 9.4, in order to define the geometric centrality of the collision. We will not follow these procedures further in this book, also since each experimental group applies a slightly different method.

In the fixed-target experiments, the longitudinal momentum is largely due to the Lorentz transformation from the CM frame to the laboratory frame. This longitudinal momentum is in general considerably greater than the transverse momentum component, and particles are focused forward along the collision axis, as seen in Fig. 5.5 [115]. In this streamer-

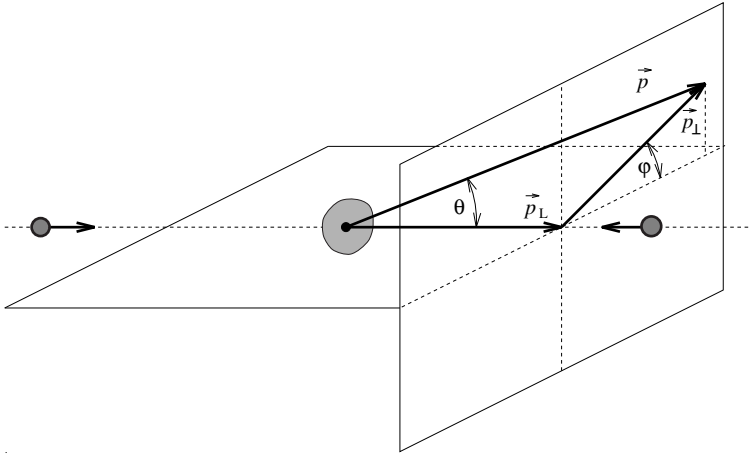


Fig. 5.6. The decomposition of particle momentum \vec{p} (shown in the CM frame) into the parallel p_L and perpendicular p_\perp components. Note the inclination angle θ of \vec{p} and the azimuthal angle φ of p_\perp (this is a qualitative presentation).

chamber picture of a S–Ag collision at 200A-GeV of the NA35 experiment, we see all particles in a cone to the right of the interaction vertex to which the charged-particle tracks are pointing. We also see that central collisions of S–Ag nuclei at 200A-GeV lead to the production of many secondary particles. Both positive and negative particles are bent in the applied magnetic field pointing normal to the plane of the picture. Several simultaneous photographs taken from various directions allowed precise tracking of charged particles.

Not all particle tracks go through the interaction vertex at the left-hand edge of Fig. 5.5: a few particle tracks, highlighted by dotted lines, belong to the V decays of neutral (strange) particles, see Fig. 2.3 on page 28. Low-momentum particles winding up as spirals in the high (1-T magnitude) magnetic field do not originate from the primary high-energy-vertex interactions.

5.3 Rapidity

We will now introduce the key kinematic variables that relate particle momentum to the dynamics that is occurring in the heavy-ion reaction. Each particle momentum decomposes, as shown in Fig. 5.6, into a longitudinal component (p_L) and a transverse component (\vec{p}_\perp) with reference to the collision axis. We note, in Fig. 5.6, the inclination angle θ of the particle against the collision axis. Also shown is the azimuthal angle φ of the two-dimensional vector \vec{p}_\perp .

The longitudinal momentum of a particle is an inconvenient variable, since it depends on the velocity of the CM frame with reference to the laboratory frame, as the appearance of Fig. 5.5 reminds us. For the analysis and understanding of the experimental results, it is necessary to be able to view the physical results from the CM frame, e.g., to transform the coordinate system to the CM frame of reference. The introduction of the rapidity y , replacing p_L , allows one to considerably simplify the selection and changing of the reference frame. This is due to the fact that the variable y is defined to be additive under successive Lorentz transformations along the same direction, as we shall see in Eq. (5.14): it can be understood as the ‘angle’ of the (hyperbolic) rotation in (3 + 1)-dimensional space. The ‘angle’ y is defined in terms of energy and momentum by the equations

$$\boxed{E = m_{\perp} \cosh y, \quad p_L = m_{\perp} \sinh y,} \quad (5.4)$$

where m_{\perp} is the transverse ‘mass’:

$$\boxed{m_{\perp} = \sqrt{m^2 + \vec{p}_{\perp}^2}.} \quad (5.5)$$

We note that Eqs. (5.4) and (5.5) are consistent with the relativistic dispersion relation (energy–momentum relation):

$$E = \sqrt{m_{\perp}^2 + p_L^2} = \sqrt{m^2 + \vec{p}_{\perp}^2 + p_L^2}. \quad (5.6)$$

The variable y (and $m_{\perp} \geq m$) replaces p_L (and $|\vec{p}_{\perp}|$), which are usually defining the momentum of a particle. The azimuthal angle φ of the vector \vec{p}_{\perp} , see Fig. 5.6, is the third variable required in the complete definition of \vec{p} .

The relation between velocity and rapidity is obtained from Eq. (5.4):

$$v_L \equiv \frac{cp_L}{E} = c \tanh y. \quad (5.7)$$

Thus, in the non-relativistic limit, $v_L \rightarrow cy$.[§] Equation (5.7) also implies that

$$\cosh y = \frac{1}{\sqrt{1 - v_L^2}} \equiv \gamma_L, \quad \sinh y = \gamma_L v_L, \quad (5.8)$$

where γ_L is the (longitudinal) Lorentz contraction factor. Since

$$\tanh^{-1} z = \frac{1}{2} \ln \left(\frac{1+z}{1-z} \right), \quad (5.9)$$

[§] Even though we like to work with units that do not explicitly introduce the velocity of light c , whenever the non-relativistic limit is discussed, it is convenient to reintroduce c explicitly into the equations, as shown above.

we obtain from Eq. (5.7)

$$y = \frac{1}{2} \ln \left(\frac{1 + v_L}{1 - v_L} \right) = \frac{1}{2} \ln \left(\frac{E + p_L}{E - p_L} \right) = \ln \left(\frac{E + p_L}{m_\perp} \right). \quad (5.10)$$

Lorentz ‘boosts’ are the Lorentz transformations with one of the three (x, y, z) Cartesian coordinate directions employed as the reference axis for the transformation. To verify the additivity of rapidity under a sequence of Lorentz boosts mentioned earlier, we consider the transformation of the momentum vector under a change of the reference frame along the collision axis. Under such a transformation, the transverse momentum and the transverse mass m_\perp are not changed. The energy and longitudinal component of momentum transform according to

$$E' = \gamma_c(E + v_c p_L), \quad p'_L = \gamma_c(p_L + v_c E). \quad (5.11)$$

Here and below, the ‘primed’ quantities are seen by an observer in the laboratory system which moves with the velocity v_c with respect to the CM frame of reference, in which the energy E and momentum p_L are measured. Noting that the rapidity y_c of the transformation satisfies Eq. (5.8), we obtain

$$\cosh y_c = \gamma_c, \quad \sinh y_c = \gamma_c v_c, \quad (5.12)$$

and, upon introducing Eq. (5.4), we find for Eq. (5.11)

$$E' = m_\perp \cosh(y + y_c), \quad p'_L = m_\perp \sinh(y + y_c). \quad (5.13)$$

It is now evident that the rapidity y' seen in the laboratory system is given in terms of the CM rapidity y by

$$y' = y + y_c. \quad (5.14)$$

It is this simple result which gives the rapidity variable its importance as a tool in the analysis of particle-production data. For example, in fixed-target experiments, we can study particle spectra using y as a variable without an explicit transformation to the CM frame of reference, and deduce from the rapidity spectra the point of symmetry corresponding to the CM rapidity. In symmetric collisions with fixed targets, the CM frame has to be in the middle between the rapidities of projectile and target; the CM rapidity is half of the rapidity of the projectile $y_{\text{CM}} = y_p/2$. In this case, the particle-rapidity spectrum must be symmetric around y_{CM} . This allows one to complement measured particle spectra: if these are available for, e.g., $y \geq y_{\text{CM}}$, a reflection at the symmetry point y_{CM} gives us the part of the spectrum with $y \leq y_{\text{CM}}$, or vice-versa.

Understanding the actual value of y_{CM} is of particular interest in ‘asymmetric’ collisions of heavy ions, i.e., those involving two different nuclei,

which we continue calling ‘projectile and target’, though such a distinction is irrelevant in our following argument, since the result will be symmetric between the two colliding nuclei. We recollect that, considering the definition Eq. (5.4), we also have

$$E \pm p_L = m_{\perp} e^{\pm y}. \tag{5.15}$$

The total energy and momentum of the colliding system is obtained from the total energy and momentum of colliding nuclei:

$$E = E^p + E^t, \quad p_L = p^p + p^t. \tag{5.16}$$

Using Eq. (5.10) for these values of E and p_L , we obtain the rapidity of the frame of reference in which the combined longitudinal momentum vanishes. For collinear collisions, the transverse momentum also vanishes, and this is the rapidity of the CM frame. Using Eq. (5.10),

$$y_{CM} = \frac{1}{2} \ln \left(\frac{E^p + E^t + p^p + p^t}{E^p + E^t - (p^p + p^t)} \right). \tag{5.17}$$

We use now Eq. (5.15) for the rapidities of projectile and target and obtain a manifestly projectile–target–symmetric expression:

$$y_{CM} = \frac{1}{2} \ln \left(\frac{m_p e^{+y_p} + m_t e^{+y_t}}{m_p e^{-y_p} + m_t e^{-y_t}} \right). \tag{5.18}$$

We now consider the asymmetric collisions both for collider and for fixed-target experiments: another way to write Eq. (5.18) offers immediate understanding of the physics involved. We take the factor e^{y_p} in the numerator and the factor e^{-y_t} in the denominator out of the logarithm and obtain

$$y_{CM} = \frac{y_p + y_t}{2} + \frac{1}{2} \ln \left(\frac{m_p + m_t e^{-(y_p - y_t)}}{m_t + m_p e^{-(y_p - y_t)}} \right). \tag{5.19}$$

In most cases of interest, we have $y_p - y_t \gg 0$ and thus

$$y_{CM} \simeq \frac{y_p + y_t}{2} - \frac{1}{2} \ln \left(\frac{m_t}{m_p} \right) + \frac{m_t^2 - m_p^2}{2m_p m_t} e^{-(y_p - y_t)} + \dots \tag{5.20}$$

In general, the first two terms largely suffice. In the way we wrote Eq. (5.20), we chose the usual convention to call the more massive nucleus the ‘target’. Two cases of explicit interest in Eq. (5.20) are the collider mode $y_p = -y_t$, and a stationary target $y_t = 0$ (up to Fermi motion in the stationary target nucleus).

For asymmetric collisions, the precise magnitude of m_t is determined in part by the value of the impact parameter, see Fig. 5.4. Hence the

CM rapidity, Eq. (5.20), becomes dependent on the impact parameter. The magnitude of the shift in asymmetry of rapidity arising can be easily estimated: in collisions in which the projectile with A_P emerges fully in the target A_T , all of the projectile nucleons participate: $A_p = A_P < A_T$, while the number of target participants A_t is

$$A_t \propto A_p^{2/3} A_T^{1/3}. \quad (5.21)$$

Thus,

$$y_{\text{CM}} \simeq \frac{y_p + y_t}{2} - \frac{1}{6} \ln \left(\frac{A_T}{A_P} \right). \quad (5.22)$$

For light-on-heavy-ion collisions such as of S on Pb, the expected and observed shift in mass asymmetry of rapidity (the last term in Eq. (5.22)) is noticeable (0.3 units).

5.4 Pseudorapidity and quasirapidity

In the study of production of charged hadrons, e.g., in section 9.2, we will see that observed particles are often not identified, and hence we do not know their masses, which are required in order to determine the rapidity of particles Eq. (5.10), given the momentum measured by deflection of particles within a magnetic field. On the other hand, mass can be negligible compared with the momenta carried by the particles, especially so in fixed-target experiments. Consequently, we now consider what happens with the rapidity spectra when the mass of a particle is small relative to the momentum, and the momentum alone determines the energy of a particle, e.g.,

$$E = \sqrt{p^2 + m^2} \rightarrow p. \quad (5.23)$$

In analogy to Eq. (5.4), a simpler variable, the ‘pseudorapidity’ η of a particle is introduced,

$$p = p_{\perp} \cosh \eta, \quad p_L = p_{\perp} \sinh \eta, \quad (5.24)$$

which, with Eq. (5.10), leads to

$$\eta = \frac{1}{2} \ln \left(\frac{p + p_L}{p - p_L} \right) = \frac{1}{2} \ln \left(\frac{1 + \cos \theta}{1 - \cos \theta} \right) = \ln \left(\cot \frac{\theta}{2} \right). \quad (5.25)$$

Here, θ is the particle-emission angle relative to the beam axis, see Fig. 5.6.

In Fig. 5.7, we see for the range of pseudorapidity of interest to us (up to $\eta = 9$, the maximum value seen in Fig. 5.1) how the angle θ varies with the pseudorapidity. A massless particle emitted transversely at $\eta = y = 0$

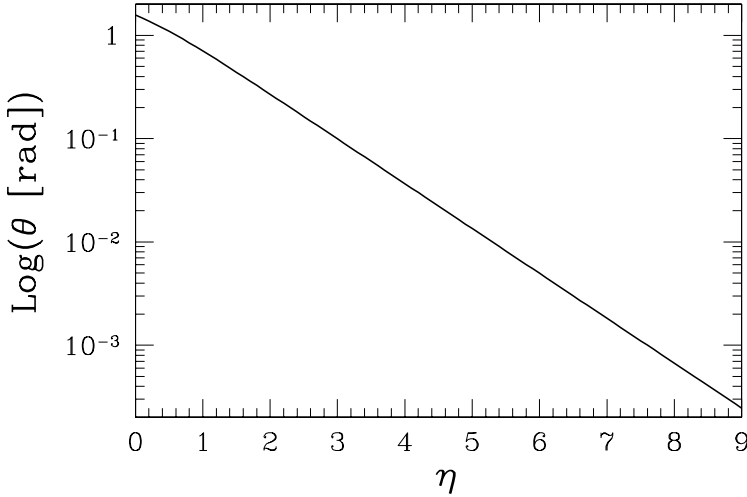


Fig. 5.7. The emission angle θ in radians as a function of the pseudorapidity η .

has $\theta = \pi/2$; $\eta = 3$ corresponds to $\theta = 0.1$ rad, ($\cong 0.1 \times 180^\circ/\pi = 5.7^\circ$). The projectile–target fragmentation region at the LHC, where $\eta \simeq 8.5$, corresponds to $\theta = \pm 4.5 \times 10^{-4}$ rad ($\cong \pm 0.025^\circ$).

From Eqs. (5.4) and (5.24), we obtain the implicit relations between pseudorapidity and rapidity:

$$\boxed{m_\perp \sinh y = p_\perp \sinh \eta, \quad E \tanh y = p \tanh \eta.} \tag{5.26}$$

We see from these relations that the pseudorapidity is always greater than the rapidity:

$$\frac{\sinh \eta}{\sinh y} = \frac{m_\perp}{p_\perp} = \sqrt{1 + \frac{m^2}{p_\perp^2}} > 1, \quad \frac{\tanh \eta}{\tanh y} = \frac{E}{p} = \sqrt{1 + \frac{m^2}{p^2}} > 1. \tag{5.27}$$

More massive particles that have not been identified appear in a pseudorapidity particle spectrum at greater values of η than do the lighter pions.

In order to establish a precise relation between pseudorapidity and rapidity, we replace in Eq. (5.25) the (longitudinal) momentum using Eqs. (5.4) and (5.6) to obtain

$$\eta = \frac{1}{2} \ln \left(\frac{\sqrt{m_\perp^2 \cosh^2 y - m^2} + m_\perp \sinh y}{\sqrt{m_\perp^2 \cosh^2 y - m^2} - m_\perp \sinh y} \right). \tag{5.28}$$

Similarly, to determine rapidity in terms of pseudorapidity, we simply replace the momenta in the definition of rapidity, Eq. (5.10), using definition Eq. (5.24):

$$y = \frac{1}{2} \ln \left(\frac{\sqrt{m^2 + p_{\perp}^2} \cosh^2 \eta + p_{\perp} \sinh \eta}{\sqrt{m^2 + p_{\perp}^2} \cosh^2 \eta - p_{\perp} \sinh \eta} \right). \quad (5.29)$$

Taking the logarithm of the first expression in Eq. (5.27), we obtain the shift in pseudorapidity relative to rapidity:

$$\delta\eta \equiv \eta - y = \frac{1}{2} \ln \left(1 + \frac{m^2}{p_{\perp}^2} \right) + \ln \left(\frac{1 - e^{-2y}}{1 - e^{-2\eta}} \right). \quad (5.30)$$

The leading term is the only term remaining for large η and it establishes an upper limit for the shift $\delta\eta$. The difference $\delta\eta = \eta - y$ between the pseudorapidity and the rapidity, as a function of pseudorapidity, is shown in Fig. 5.8, which was obtained by inserting Eq. (5.29) into Eq. (5.30). Thick lines are for $p_{\perp} = 0.3$ GeV, thin lines for $p_{\perp} = 0.5$ GeV; solid lines are for nucleons, chain lines for kaons, and dashed lines for pions. We see that, when $\eta \geq 3$, the first term in Eq. (5.30) in fact suffices to approximate the ‘shift’ in pseudorapidity which approaches a fixed maximum.

For sufficiently large $p_{\perp} > m$, when a particle’s rest mass can be neglected, the shift $\delta\eta$ becomes negligible. For pions the error associated with considering the pseudorapidity instead of rapidity in hadronic reactions can often be ignored since the mass is usually smaller than the typical momentum cut – and thus $\delta\eta < 0.1$ is seen at pseudorapidity $\eta = 3$ for $p_{\perp} > 0.3$ GeV. Moreover, the use of pion-quasirapidity y_{π} , which we discuss next, eliminates this shift completely. On the other hand, use of pseudorapidity seems not to be advisable for situations in which contributions from more massive particles are of importance, unless, as Eq. (5.30) suggests, the p_{\perp} cut is well above the mass of the particle. We see, in Fig. 5.8, that, for nucleons, taking the transverse momentum cut at 0.3 GeV, one encounters a shift of more than one rapidity unit at $\eta = 3$, the SPS value.

Since, in the upper SPS energy range (see table 5.1), the pion abundance dominates the hadron abundance, it has become common practice to show the distribution of hadrons as a function of pion-quasirapidity y_{π} , presuming that all hadrons observed are pions, as is done in Fig. 9.6 on page 166. One assumes, in lieu of the correct definition for each particle, the expression as if this particle had the mass of a pion:

$$p_L = p_{\perp} \sinh \eta \rightarrow p_L = \sqrt{p_{\perp}^2 + m_{\pi}^2} \sinh y_{\pi}. \quad (5.31)$$

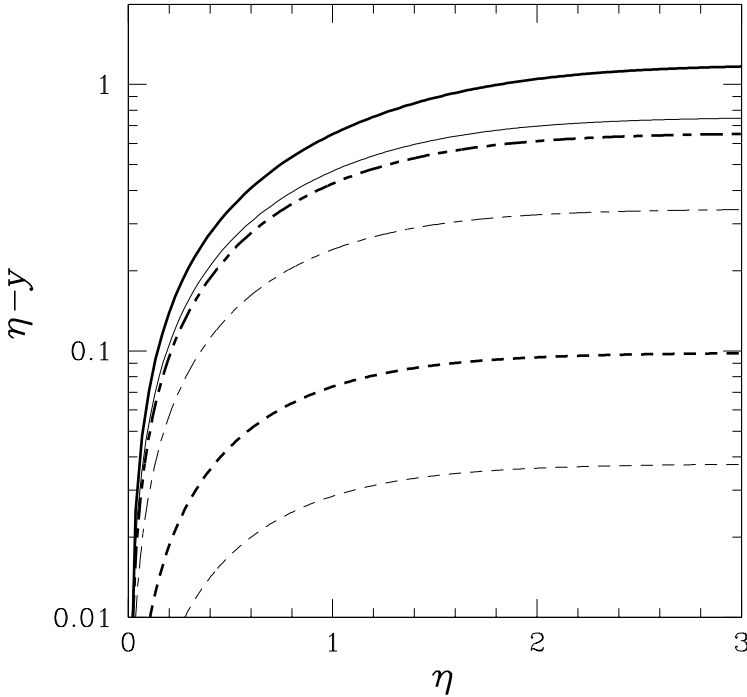


Fig. 5.8. The difference between pseudorapidity and pion-quasirapidity π (dashed lines), kaons K (chain lines), and nucleons N (solid lines) as a function of pseudorapidity η , for $p_{\perp} = 0.3$ GeV (thick lines) and $p_{\perp} = 0.5$ GeV (thin lines).

Following the derivation of Eq. (5.30), we obtain

$$\delta y \equiv y_{\pi} - y = \frac{1}{2} \ln \left(1 + \frac{m^2 - m_{\pi}^2}{p_{\perp}^2 + m_{\pi}^2} \right) + \ln \left(\frac{1 - e^{-2y}}{1 - e^{-2y_{\pi}}} \right). \quad (5.32)$$

In Fig. 5.9, we see the solution of the above equation as a function of the pion-quasirapidity. Lines are for $p_{\perp} = 0.5$ GeV (bottom line, smallest shift), $p_{\perp} = 0.3$ GeV (middle line), and for $p_{\perp} = 0.1$ GeV (top, largest shift); solid lines are for nucleons and chain lines for kaons. Again, when $\delta y \geq 3$, the first term in Eq. (5.32) nearly suffices to approximate the ‘shift’ in rapidity for pions as shown in Fig. 5.9 for increasing y_{π} , it approaches a fixed value, which for $p_{\perp} < m_{\pi}$ is significant. The quasirapidity distribution for nucleons experiences a widening by ± 1.9 , and that for kaons widens by ± 1.3 units of rapidity.

As we see in Figs. 5.8 and 5.9 and Eqs. (5.30) and (5.32), the error in measurement of rapidity grows with decreasing p_{\perp} of the particle. For kaons and nucleons, in the range of p_{\perp} within which the pseudorapidity is

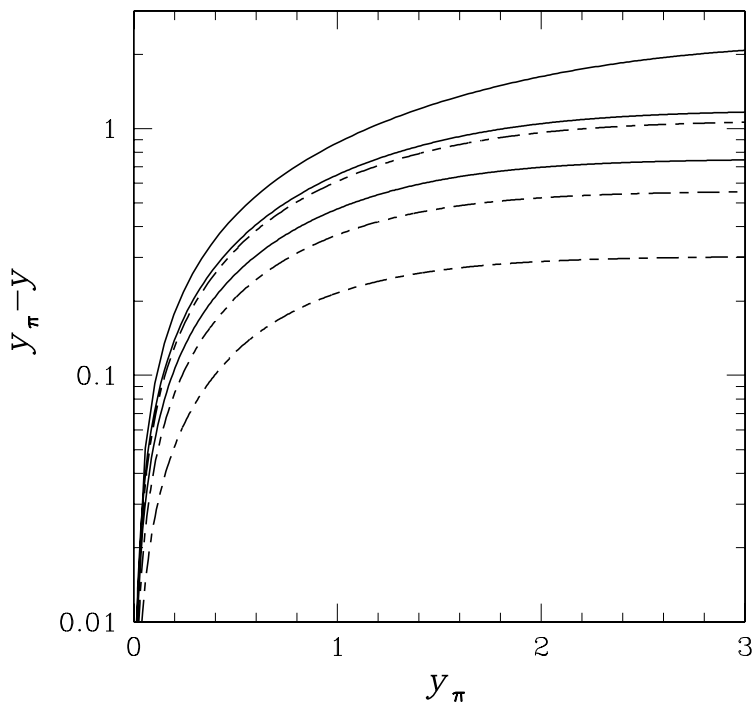


Fig. 5.9. The difference between pion-quasirapidity and rapidity as a function of quasirapidity y_π for kaons K (chain lines), and nucleons N (solid lines), from bottom to top for $p_\perp = 0.5$ GeV, $p_\perp = 0.3$ GeV, and $p_\perp = 0.1$ GeV.

failing to be a good variable, the number of particles produced increases with decreasing p_\perp . Thus, in fact, use of pseudorapidity or quasirapidity can be significantly misleading when one wants to understand both the spectral shape and the hadron yield.

In this context, we recall that a study of the distribution of heavy particles (nucleons and kaons) can be based on the difference between the distributions of positively and negatively charged particles, which is relatively easy to measure:

$$\frac{d(N^+ - N^-)}{dy_\pi} = \frac{d(\pi^+ - \pi^-)}{dy_\pi} + \frac{d(p - \bar{p})}{dy_\pi} + \frac{d(K^+ - K^-)}{dy_\pi}. \quad (5.33)$$

The physics, in Eq. (5.33), is that the yield of pions is nearly charge symmetric (this has been observed at the SPS for $p_\perp > 0.3$ GeV [77]) and the first term cancels out. In the remainder, we have an initial measure of the quasirapidity distribution of protons and kaons. At the SPS, both protons and kaons contribute in Eq. (5.33). At the RHIC, the abundance of charged kaons is the dominating contribution, but only at the level of 1%-3% of all charged particles. As noted above, at the SPS, the canceling

out of charged-pion yield is not exact at low $p_{\perp} < 0.25$ GeV, as a direct measurement has shown [77]: in the Pb–Pb collision system, we have 20% $(n - p)/(n + p)$ asymmetry in the number of protons and neutrons. This charge asymmetry translates into a relatively strong π^+/π^- asymmetry at small p_{\perp} , but disappears for $p_{\perp} > 0.2$ GeV.

5.5 Stages of evolution of dense matter

Since hadronic interactions are strong, we can hope and expect that local equilibrium conditions can be approached in experiments involving heavy ions. This is in particular the case if we characterize the essential physical properties of elementary matter in term of local, position-dependent parameters. The local average energy of each particle characterizes the local temperature T . (Local) chemical potentials μ_i need to be introduced in order to regulate the average particle and/or quark-flavor density.

These parameters express different equilibration processes in the fireball, and in general there is a considerable difference between thermal and chemical equilibrium.

- In order to establish thermal equilibrium, equipartition of energy among the different particles present has to occur in the collisional processes which lead to the statistical energy distribution. It is important to note that (local) thermal equilibrium can be achieved solely by elastic scattering. We will call the time scale on which these processes occur τ_{th} . The use of temperature T as a parameter presupposes that thermal equilibrium has (nearly) been established.
- Chemical equilibration requires reactions that change numbers of particles, and it is more difficult and thus slower to become established. There are also two quite different types of chemical equilibria.

— *Relative* chemical equilibration, just like the commonly known case in chemistry, involves reactions that distribute a certain already existent element/property among different accessible compounds. Use of chemical potentials μ_i presupposes, in general, that the particular relative chemical equilibrium is being considered. We call the relevant time scale $\tau_{\text{chem}}^{\text{rel}}$.

— In relativistic reactions, particles can be made as energy is converted into matter. Therefore, we can expect to approach (more slowly) the *absolute* chemical equilibrium. We call the relevant time scale $\tau_{\text{chem}}^{\text{abs}}$. We characterize the approach to absolute chemical equilibrium by a fugacity factor γ_i for particle ‘ i ’. We often study the evolution of γ_i in the collision as a function of time, since absolute chemical equilibrium cannot generally be assumed to occur.

Some authors introduce separate chemical potentials for particles and antiparticles, $\mu_i^\pm = \pm\mu_i + T \ln \gamma_i$, [188, 189]. This is equivalent to our approach. However, it is still common to see in the literature that an equilibrium is assumed, $\gamma_i = 1$, with particles ‘instantaneously’ reaching their absolute chemical-equilibrium abundances. Such an approach cannot in general be justified. We see this on considering the relation between the relaxation times,

$$10^{-22} \text{ s} > \tau^{\text{exp}} \simeq \tau_{\text{chem}}^{\text{abs}} > \tau_{\text{chem}}^{\text{rel}} > \tau_{\text{th}}, \quad (5.34)$$

where τ^{exp} is the life span of the expanding fireball of dense matter, which is of the same magnitude as the time light needs to traverse the largest nuclei. In such a rapidly evolving system, we cannot assume that absolute chemical equilibrium, $\gamma_i = 1$, has been attained.

In order to illustrate the difference between absolute and relative chemical equilibrium better, let us consider some examples.

- We consider the baryon number, the globally conserved property of dense hadronic matter. Locally, the global conservation implies a balance of inflow against outflow, viz., there are no sources or sinks of baryon number. Generally, one always associates a conserved quantity with the presence of a chemical potential, here the chemical potential μ_b which controls the difference in number of all baryons and antibaryons. A change in the energy of the system, according to the first law of thermodynamics, is then given by

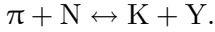
$$dE = -P dV + T dS + \mu_b db. \quad (5.35)$$

However, the addition of a baryon–antibaryon pair to the system will not be noted in Eq. (5.35), since the baryon number b remains unchanged!

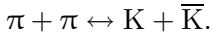
At this point, we are not at liberty to add or remove a pair: in writing down Eq. (5.35), we *implicitly* assumed what we have above called absolute chemical equilibrium – there is a bath of baryon number in which our system is immersed, and hence a full phase-space occupancy of all available phase-space cells, and there is no place for an extra pair. By changing the chemical potential μ_b , we can regulate the difference in number of baryons and antibaryons present in the system, but densities of baryons and antibaryons move together, absolute equilibrium is assumed while relative chemical equilibrium controls the relative number of particles by virtue of the value of the chemical potential. If we change the baryon number by one at fixed volume and entropy, then according to Eq. (5.35), there is a change in energy by μ_b .

- Next, we look at the abundance of strangeness in the baryon-rich HG phase. There is no strangeness ‘bath’ and, initially, we have no strangeness, therefore we will be making pairs of s and \bar{s} quarks; there is plenty of phase space available to fill, and we are far from absolute

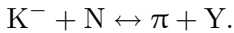
chemical-strangeness equilibrium. To make $s\bar{s}$ pairs in a HG, there are many possible reactions, section 18.2, classified usually as the direct- and associate-production processes. In the associate-production process, a pair of strange quarks is shared between two existent hadrons, of which one is a baryon, typically a nucleon N, which becomes a hyperon Y:



In a direct-production process, a pair of strangeness-carrying particles is formed directly via annihilation of two mesons, akin to our *Gedankenexperiment* in which we are adding a pair to the system:



Here, a pair of strange particles is made in the form of a pair of kaons, K^+K^- . With these two reaction types alone it could be that populations of strange mesons and baryons evolve differently. However, the meson carrier of the s quark, K^- , can exchange this quark rather fast, via exothermic reaction with a nucleon, forming a hyperon:



This reaction establishes relative chemical equilibrium by being able to move the strange quark between the two different carriers, $s\bar{q}$ mesons and sq baryons.

Reactions establishing the redistribution of existent flavor, or the abundance of some other conserved quantity, play a different role from the reactions that actually contribute to the formation of this flavor, or other quantum number, and facilitate the approach to absolute chemical equilibrium. Accordingly, the time constants for relaxation are different, since different types of reaction are involved.

Apart from the different relaxation times associated with the different types of thermal and chemical equilibria, there are different time scales associated with the different fundamental interactions involved. For example, the electro-magnetic interactions are considerably slower at reaching equilibrium than are the strong interactions governing the evolution of dense hadronic fireballs created in ultra-relativistic heavy-ion collisions. All the important time constants for relaxation in heavy-ion collisions arise from differences in mechanisms operating within the realm of strong interactions. Therefore, the separation of time scales is not as sharp as that between the different interactions, though a clear hierarchy arises, as we noted in Eq. (5.34).

Under weak interactions, there is, in comparison, an extremely slow transmutation of quark (and lepton) flavors, involving a much longer electro-weak equilibration time. Such long times are not available in the

micro-bang process, in contrast to the big-bang case. We considered these electro-weak degrees of freedom in section 1.3, since the life span of the Universe at the time of the hadronic phase transition exceeds all typical relaxation times for the weak interaction.

The chemical equilibration, and hence the chemical composition of the fireball, evolve along with the temperature of the fireball. The following stages occur in heavy-ion collision.

1. The initial quantum stage.

The formation of a thermalized state within τ_{th} is most difficult to understand, and is subject to intense current theoretical investigation. During the pre-thermal time, $0 \leq t < \tau_{\text{th}}$, the properties of the collision system require the study both of quantum transport and of decoherence phenomena, a subject reaching today far beyond the scope of this volume. We assume, in this book, that the thermal shape of a (quark, gluon) particle-momentum distribution is reached instantaneously compared with the time scales for chemical equilibration in Eq. (5.34). This allows us to sidestep questions regarding the dynamics occurring in the first moments of the heavy-ion interactions, and we explore primarily what happens after a time[¶] $\tau_0 \equiv \tau_{\text{th}} \simeq 0.25\text{--}1 \text{ fm}/c$. The value of τ_0 decreases as the density of the pre-thermal initial state increases, e.g., as the collision energy increases. At τ_0 gluons g are, due to their greater reactivity, at or near to the local chemical equilibrium.

2. The subsequent chemical equilibration time.

During the inter-penetration of the projectile and the target lasting no less than $\sim 1.5 \text{ fm}/c$, diverse particle-production reactions occur, allowing the approach to chemical equilibrium by light non-strange quarks $q = u, d$. As the energy is redistributed among an increasing number of accessed degrees of freedom, the temperature drops rapidly.

3. The strangeness chemical equilibration.

A third time period, lasting up to $\simeq 5 \text{ fm}/c$, during which the production and chemical equilibration of strange quarks takes place. There is a reduction of temperature now mainly due to the expansion flow, though the excitation of the strange quark degree of freedom also introduces a non-negligible cooling effect.

4. The hadronization/freeze-out.

The fireball of dense matter expands and decomposes into the final-state hadrons, possibly in an (explosive) process that does not allow re-equilibration of the final-state particles. The dynamics is strongly dependent on the size of the initial state and on the nature of the equations of state.

[¶] The time τ_{th} is often called τ_0 in the literature, and we will use this notation as well, though the subscript ‘th’ is more specific about the evolution step considered.

Throughout these stages, a local thermal equilibrium is rapidly established and, as noted, the local temperature evolves in time to accommodate change in the internal structure as is appropriate for an isolated physical system. We have a temperature evolution that passes through these series of stages:

- T_{th} the temperature associated with the initial thermal equilibrium,
- ↓ *evolution dominated mainly by production of q and \bar{q} ;*
- T_{ch} chemical equilibrium of non-strange quarks and gluons,
- ↓ *evolution dominated by expansion and production of s and \bar{s} ;*
- T_{s} condition of chemical equilibrium of u , d and s quark flavors,
- ↓ *expansion, dissociation by particle radiation;*
- T_{f} temperature at hadron-abundance freeze-out,
- ↓ *hadron rescattering, reequilibration; and*
- T_{tf} temperature at thermal freeze-out, $T = T(\tau^{\text{exp}})$.

We encounter a considerable decrease in temperature. The entropy content of an evolving isolated system must increase, and this is initially related to the increase in the number of particles within the fireball and later also due to the increase in volume. However, in the later stages dominated by flow, the practical absence of viscosities in the quark–gluon fluid implies that there is little additional production of entropy. The final entropy content is close to the entropy content established in the earliest thermal stage of the collision at $t < \tau_0$, despite a drop in temperature by as much as a factor of two (under current experimental RHIC conditions) during the evolution of the fireball.

Except for the unlikely scenario of a fireball not expanding, but suddenly disintegrating, none of the temperatures discussed above corresponds to the temperature one would read off the (inverse) slopes of particle spectra. In principle, the freeze-out temperature determines the shape of emission and multiplicity of emitted particles. However, the freeze-out occurs within a local flow field of expanding matter and the thermal spectrum is to be folded with the flow which imposes a Doppler-like shift of T_{tf} : we observe a higher temperature than is actually locally present when particles decouple from flowing matter (kinetic or thermal freeze-out). The observable temperature T_{\perp} is related to the intrinsic temperature of the source:

$$T_{\perp} \simeq \frac{1 + \vec{n} \cdot \vec{v}_{\text{tf}}}{\sqrt{1 - v_{\text{f}}^2}} T_{\text{tf}} \rightarrow \sqrt{\frac{1 + v_{\text{tf}}}{1 - v_{\text{tf}}}} T_{\text{tf}}. \quad (5.36)$$

This relation must be used with caution, since it does not apply in the same fashion to all particles and has a precision rarely better than $\pm 10\%$. We study the shape of m_{\perp} -spectra in section 8.5.

5.6 Approach to local kinetic equilibrium

In the above discussion, the formation of a space–time-localized fireball of dense matter is the first key physics input. The question we wish to address now is that of how this fireball can possibly arise from a rather short sequence of individual reactions that occur when two, rather small, gas clouds of partons, clustered in nucleons, bound in the nucleus, collide. Indeed, at first sight, one would be led to believe that the small clouds comprising point-like objects would mutually disperse in the collision, and no localized, dense state of hadronic matter should be formed. At best, it was suggested in some early work, the two colliding ‘eggs’ should emerge from the high-energy interaction slightly ‘warmed’, but still largely ‘unbroken’.

Two remarkable properties of hadronic interactions are responsible for just the opposite, deeply inelastic, behavior:

- the multiparticle production in hadron–hadron collisions; and
- the effective size of all hadrons expressed in term of their reaction cross sections.

What appears to be a thin system of point-like constituents is effectively already a volume-filling nucleon liquid, which will undergo, in a collision, a rapid self-multiplication with particle density rising and individual scattering times becoming progressively much shorter than the overall collision time.

Ultimately, as the energy available in collision is increased, the hadron particle/energy density will reach values at which the dissolution of the hadronic constituents into a common deconfined domain will become possible, and indeed must occur according to our knowledge about strong interactions. While we do not really know whether deconfinement of hadrons is not a general mechanism operating already at AGS energies, see table 5.1, there is today no experimental evidence that this low-energy range suffices. In contradistinction, a significant number of results obtained at the SPS energy range can be most naturally interpreted in terms of the formation of a deconfined space–time domain, section 1.6. We note that, per participant, there are as many as 7–10 further hadrons produced at SPS energies. This implies that there are thousands of quarks and gluons in the space–time domain of interest, and hence consideration of a ‘local’ (in space–time) equilibrium makes good sense.

There are many ways to estimate the particle number. We can use the number of final-state hadrons and evaluate the numbers of constituent quarks and antiquarks, or we can take the available energy content and divide it by the estimated energy per particle (quark, gluon). Both procedures give $\mathcal{O}(10\,000)$ particles for the case of Pb–Pb collisions at 158.4-GeV ($\sqrt{s_{NN}} = 17.2$ GeV). Of these, not all particles can be causally

connected, i.e., not all these particles can influence each other in classical dynamics, and local equilibrium is a feature obviously involving a causally connected region only.

A suitable measure of the causally connected size is offered by the initial decoherence time τ_0 , which also determines the size of the decoherence volume, $R_0 \simeq \tau_0$. This has to be scaled up by the ensuing expansion factor, see the discussion below Eq. (6.35). For $\tau_0 = 0.5$ fm, we can expect about 5%–10% of all particles (500–1000) to be causally connected, which implies that the causal ‘range’ of rapidity is an interval $\Delta y \simeq 1$. Δy arises on considering the final-state rapidity distribution, see Fig. 9.6 on page 166 and Fig. 9.19 on page 184. In any case, the concept of a local equilibrium makes good sense.

When we are talking about thermal equilibria, we must first establish more precisely what these words mean. We will implicitly always refer to ‘local’ equilibrium. The thermalization of the momentum distributions is driven by *all* scattering processes, elastic as well as inelastic, because all of them are associated with transfer of momentum and energy between particles. The *scattering time scale*, for particles of species i , is given in terms of the collision length l by

$$\tau_{i,\text{scatt}} = \left\langle \frac{l}{v} \right\rangle_i = \frac{1}{\sum_j \langle \sigma_{ij} v_{ij} \rangle \rho_j}, \quad (5.37)$$

where the sum in the denominator is over all particle species (with densities ρ_j) available, σ_{ij} and v_{ij} are the (energy-dependent) total cross sections and relative velocities, for a process scattering particles i and j , and the average is to be taken over the momentum distributions of the particle considered.

It is not hard to ‘guestimate’ the time scale governing the kinetic equilibration in the QGP. The typical particle-collision time (the inverse of the collision frequency) is obtained from Eq. (5.37) above. Given the particle densities and soft reaction cross sections, with the relative velocity of these essentially massless components being the velocity of light c , we find for the QGP scattering time,

$$\tau_i^{\text{QGP}} = 0.2\text{--}2 \text{ fm}, \quad \text{with } \rho_i = 2\text{--}10 \text{ fm}^{-3}, \quad \sigma_i = 2\text{--}5 \text{ mb}, \quad (5.38)$$

as a range for different particles of type i , with the shorter time applying to the early high-density stage. This is about an order of magnitude shorter than the time scale for evolution of the fireball, which is derived from the spatial size of the colliding system: for the largest nuclei, in particular the Pb–Pb or Au–Au collisions, over a wide range of energy, we expect

$$\tau^{\text{exp}} \simeq \frac{R_A}{c} \simeq 5\text{--}8 \text{ fm}/c. \quad (5.39)$$

The achievement of kinetic equilibrium must be visible in the energy spectra of the particles produced, as we shall discuss below in section 8.1. This behavior, as we argue, can be understood in qualitative terms for the case of nuclear collisions. However, it remains to date a mystery why in some important aspects thermal models succeed for the case of p–p reactions. In particular, the exponential fall off of particle spectra, suggesting thermal equilibrium, has been noted with trepidation for a considerable time.

Hagedorn evaluated this behavior in the experimental data some 35 years ago [140, 145] and he developed the statistical bootstrap model (chapter 12), which assumes a statistical phase-space distribution (section 12.2). Hagedorn called it *preestablished or preformed equilibrium*: particles are produced in an elementary interaction with a probability characterized by a universal temperature. We can today only speculate about the physical mechanisms.

For example, it has been proposed that vacuum-structure fluctuations lead to color-string tension fluctuation, and thus the resulting string-breaking produces thermal hadrons [65]. Another informally discussed possibility is the presence of intrinsic chaotic dynamics capable of rapidly establishing kinetic equilibrium. We cannot pursue further in this book these ideas about the process of initial thermal equilibration.

Sometimes, the fact that we do not fully understand thermalization in the p–p case is raised as an argument against the possibility of conventional equilibration in nuclear collisions. We do not think so. In fact, if the p–p case leads to thermal hadrons, we should have a yet better thermalization in the A–A case. Thus, a microscopic model that is adopted to extrapolate from p–p to A–A collisions should respect the concept of the hadronic preestablished equilibrium, else it is not going to be fully successful, see section 6.1.

5.7 The approach to chemical equilibrium

The approach to chemical equilibrium is, in comparison with the thermal case, better understood. Firstly, we must consider which particles can be expected to have reached equilibrium and which not, and this requires a kinetic description. Though, in general, one is tempted to think of a build-up of chemical abundance of different quark flavors, the approach to absolute chemical equilibrium need not always occur from ‘below’, and/or the measured quark yields can be in excess of chemical equilibrium; section 19.4.

At the collision energies available at the RHIC and LHC, the more massive charm c and bottom b quarks (see table 1.1) are produced in the initial interaction, reaching and even exceeding the yield expected in

absolute chemical equilibrium in thermalized deconfined matter. In QGP the chemical equilibration of these flavors occurs exceedingly slowly, and a significant excess of abundance is expected. A similar situation can arise with strangeness in presence of rapid cooling, from $T > 250$ MeV to $T \simeq 150$ MeV, which preserves the high initial thermal yield. In the early Universe, the well-known example of chemical nonequilibrium occurring, despite thermal equilibrium being established, is the freeze-out of abundances of light nuclear isotopes.

Of particular interest, in the physics of QGP, is that the saturation ('absolute' chemical equilibration) of the phase space of strange particles requires just the life span of the QGP. This is, in part, due to the relatively large threshold for the production of strange quarks and, in part, because for practical purposes most strangeness needs to be produced in thermal energy collisions – direct initial-state production of strangeness is of course quite prevalent but at the level of 10%–30% of the final-state equilibrium yield of strangeness, as long as only the normal processes of hadron collisions contribute to direct production of strangeness.

In the QGP phase, there is no need to redistribute strange quarks among different carriers and relative chemical equilibrium is automatically established. More generally, in the HG phase the relative chemical equilibrium is more easily attained than is the 'absolute' chemical equilibrium, due to the strangeness-exchange cross sections being greater than cross sections for its production.

The population master equation,

$$\frac{2\tau_{\text{chem}}^i}{\rho_i^{\text{eq}}} \frac{d\rho_i}{dt} = 1 - \left(\frac{\rho_i}{\rho_i^{\text{eq}}} \right)^2, \quad (5.40)$$

describes the population evolution of strangeness (and charm, etc.) within the scattering theory; chapter 17. τ_{chem}^i is the time constant for chemical relaxation. The quadratic term on the right-hand side, in Eq. (5.40), arises from, e.g., annihilation of strangeness, $s\bar{s} \rightarrow XX$, which rate is established by detailed balance consideration of two-body reactions. In the first instance, one has not ρ_i^2 but $\rho_i\bar{\rho}_i$, where $\bar{\rho}_i$ is the \bar{s} density. However, since in heavy-ion collisions only hadronic reactions produce strangeness, we maintain the condition $\rho_i = \bar{\rho}_i$ and Eq. (5.40) follows. The solution of Eq. (5.40) approaches equilibrium exponentially for $t \rightarrow \infty$:

$$\rho_i = \rho_i^{\text{eq}} \tanh[t/(2\tau_{\text{chem}}^i)] \rightarrow (1 - e^{-t/\tau_{\text{chem}}^i})\rho_i^{\text{eq}}. \quad (5.41)$$

The chemical equilibration (relaxation) time constant τ_{chem}^i , for particle species i , is computed as an inverse of the invariant reaction rate per unit volume R_i :

$$\tau_{\text{chem}}^i = \frac{\rho_i^{\text{eq}}}{2R_i}. \quad (5.42)$$

In Eq. (5.42), ρ_i^{eq} is the chemical-equilibrium density. R_i is the rate at which the system ‘chases’ ρ_i^{eq} ; the ratio is a characteristic time when the chase is over. The factor 2 in Eq. (5.42) is introduced to assure that the approach to equilibrium due to two-body reactions is governed by an exponential function with the time-decay parameter τ_{chem}^i , as is seen on the right-hand side of Eq. (5.41).

In terms of the reaction cross section, the invariant reaction rate per unit of time and volume is obtained from (see section 17.1)

$$R_i(x) = \sum_{a,b,X} \int_{(m_i+m_X)^2}^{\infty} 2\lambda_2(s) ds \int \frac{d^3k_a}{(2\pi)^3 2E_a} \int \frac{d^3k_b}{(2\pi)^3 2E_b} \times f_a(k_a, x) f_b(k_b, x) \bar{\sigma}_{ab \rightarrow iX}(\sqrt{s}) \delta[s - (k_a + k_b)^2]. \quad (5.43)$$

where, see Eq. (17.10),

$$\lambda_2(s) = [s - (m_a + m_b)^2][s - (m_a - m_b)^2].$$

In Eq. (5.43), we are neglecting Pauli or Bose quantum effects (suppression or stimulated-emission factors) in the initial and final states. Considered here, is the inelastic production process $a + b \rightarrow i + X$. $f_a(k_a, x)$ and $f_b(k_b, x)$ are the phase-space distributions of the colliding particles, and $\bar{\sigma}_{ab \rightarrow iX}(\sqrt{s})$ is the energy-dependent cross section for this inelastic channel. The ‘bar’ indicates that the dependence on transfer of momentum (scattering angle) is averaged over.

We will further study this integral for thermal distributions in section 17.1. However, given the importance of the final result Eq. (17.16), we record it here for the simplest case of a relativistic Boltzmann momentum distribution,

$$R_i(x) = \frac{\sum_{a,b,X} \int_{w_0}^{\infty} dw \lambda_2 \bar{\sigma}_{ab \rightarrow iX}(w) K_1(w/T)}{4T m_a^2 m_b^2 K_2(m_a/T) K_2(m_b/T)}, \quad (5.44)$$

where $w = \sqrt{s}$ is the CM energy and $w_0 = m_i + m_X$ is the reaction threshold. This formula is presented in this form in [164], Eq. (5.7); it is stated there for the special case in which the reacting particles a and b are identical bosons, which, to avoid double counting of indistinguishable pairs of particles, requires an extra factor $\frac{1}{2}$, which is not included in Eq. (5.44). The interesting $m_{a,b} \rightarrow 0$ limit follows considering Fig. 10.1 and Eq. (10.47). It is implemented with a replacement of each factor $m^2 K_2(m/T)$ by $2T^2$ in Eq. (5.44), and $\lambda_2 \rightarrow s$, which reduces Eq. (5.44) to the result presented in [226], Eq. (2); [67] lacks the factor $1/T$.

We see explicitly, in Eq. (5.44), the mass threshold in the s -integration occurring for inelastic (particle-producing) rates. A high threshold combines with the exponentially small K_1 Bessel function, see Eq. (8.7), to

reduce the strength of inelastic hadronic particle-production rates, which are usually much smaller than the total rates of reaction (scattering). For this reason, the time scale of chemical equilibration is, in general, considerably longer than the thermal one.

6 Understanding collision dynamics

6.1 Cascades of particles

The principal shortcomings of the near-statistical-equilibrium method, combined with ideal flow of hadronic fluid in the study of heavy-ion collisions, are the following:

- we do not have a long-lived, large region of hot hadronic matter to look at, and some features of the collision are certainly not well equilibrated;
- we need to establish the physical conditions at the initial time τ_0 ; and
- the system considered is subject to rapid evolution and all thermal properties are actually fields, i.e., we have a position-dependent local temperature $T(\vec{x})$, etc.

Hence, a lot of effort continues to be committed to the development of a better understanding of the initial interaction dynamics, and its subsequent description within microscopic kinetic-scattering models. The research field of the study of computer-code ‘event generators’ is vast and undergoing development. Consequently, in this book, we will enter into discussion of kinetic models only as matters of example and/or principle. We survey the rapidly developing field in order to offer an entry point for further study.

For a novice in this very rapidly changing panorama, the best next step is to look at the progress of the working group which has been monitoring the development of the computer codes with the objective of ensuring that reasonable quality control is attained.

OSCAR (Open Standard Codes and Routines)^{||}. OSCAR began in June 1997 to resolve the lack of common standards, documentation, version control, and accessibility in many transport codes. These transport codes for relativistic heavy-ion collisions differ from computer codes in other areas of physics, where numerical methods are only technical tools used to solve specific equations that define the physics. The source code of a nuclear-collision transport model often implements extra physical assumptions and dynamic mechanisms that go beyond the equations used to motivate its design. These algorithms often undergo evolution with time, and the very large number of phenomenological parameters also

^{||} See: <http://www.cunuke.phys.columbia.edu/people/molnard/mirror-OSCAR/oscar>.